Stability Analysis of Real-World Subsynchronous Oscillations via Black-Box EMT Models

Rahul Halugudde Ramakrishna, *Student Member, IEEE*, Zhixin Miao, *Senior Member, IEEE*, Lingling Fan, *Fellow, IEEE*

Abstract—In this paper, we demonstrate methods to extract dq admittance for a solar photovoltaic (PV) farm from its black-box model used for electromagnetic transient (EMT) simulation. Each dq admittance corresponds to a certain operating condition. Based on the dq admittance, analysis is carried out to evaluate how grid strength and solar irradiance may influence stability. Two types of stability analysis methods (open-loop system based and closed-loop system based) are examined and both can deal with dq admittance's frequency-domain measurements directly and produce graphics for stability analysis. The findings based on dq admittance-based analysis are shown to corroborate EMT simulation results.

Index Terms—Inverter-based resources, sub-synchronous oscillations, stability analysis, weak grid, admittance.

I. INTRODUCTION

POWER grids worldwide have experienced a significant amount of inverter-based resource (IBR) interconnections. In many regions of low grid strength, subsynchronous oscillations (SSO) have been observed. Among the real-world SSO events documented in the IEEE PES IBR SSO taskforce paper [1], 15 out of 19 events are associated with low grid strength. While some of those oscillations do not cause immediate reliability concerns, they may lead to uncontrolled tripping of IBRs in extremely weak grid scenarios. Additionally, oscillations may be introduced by solar PV power plant-level voltage and frequency control, which relies on communication systems to send commands to individual inverters [2]. Hence, screening for possible SSO is imperative.

We can determine the system's stability using eigenvalues based on state-space analytical models [3], [4]. The state-space analytical models for three-phase grid-integrated IBRs are based on dq frames and their state variables at steady state are all constants. This feature of the analytical models enables Jacobian linearization of the dynamical system at an operating condition through efficient numerical perturbation techniques widely available. On the other hand, what the system operators have are generally black-box models for EMT simulation from vendors and stability check relying on such models has a major challenge besides the modeling blocks being not transparent. The black-box models are based on the static abc frame and their state variables are periodic at steady state. Therefore, it is not possible to extract a linear model directly from the black-box EMT models via Jacobian linearization.

To this end, we resort to an alternative method to extract linear models. This method is based on frequency-domain

impedance/admittance (either scalar or dq-frame based) and those frequency responses can be found by frequency scans (sinusoidal perturbation) or other perturbations. The impedance-based method has been used in stability analysis for a while. In the 1976 paper by Undrill and Kostyniak [5], the frequency scanning method has been applied for synchronous generator SSO analysis. A power grid is broke into two subsystems (a generator and the rest of the network), and each subsystem is subject to sinusoidal perturbations in voltage or current. This method leads to two linear subsystems of a feedback system. The method has found many applications for the current-day IBR penetrated power grids, *e.g.*, the scalar impedance or positive-sequence impedance based analysis has been used to study the sub-synchronous interaction between a type-3 wind farm and series compensated line [6], [7].

For more accurate analysis, the dq-admittance's frequency responses may be fitted to a parametric model. We may perform vector fitting [8] on the frequency response measurements to obtain a multi-input, multi-output (MIMO) model either in the transfer function matrix or the state-space form. Based on the s-domain model, we may find eigenvalues and frequency-domain mode shapes to identify the influencing factors for an oscillation mode [9].

Additionally, the dq-admittance's frequency responses can be directly used for stability analysis through visual examination, thereby saving the effort of fitting the frequency-domain responses to a parametric model. This straightforward approach is based on the Generalized Nyquist Criterion (GNC). A system is first viewed as two blocks at the IBR's point of interconnection, with one block representing the admittance of the IBR and the other block representing the grid impedance. Their product is the open-loop gain and GNC will be applied on this loop gain for stability analysis [10]–[12].

A. Objectives

The aim of this paper is to examine the influencing factors on real-world SSO events by use of black-box EMT models of a real-world 80-MW solar farm. The SSO events in the frequency range of 17-20 Hz have been observed in the Australian network and EMT simulation-based replication studies by use of black-box EMT models have been successful [13]. Instead of focusing on EMT simulation studies, this paper focuses on stability analysis. With the black-box EMT models of IBR, dq admittance of the IBR will be extracted. Subsequently, we will investigate the effect of solar irradiance and the grid strength on SSO via dq admittance-based analysis.

B. Our contributions

DQ-admittance-based stability analysis relies on frequency response measurement data rather than on a detailed simulation model. This feature is unique. However, acquiring frequency response measurement data is time consuming. (i) In this paper, we recommend the best practices for accurate measurement. Specifically, we share critical steps to be included while setting up the measurement test bed and during the data acquisition process. We compare two types of measurement testbeds based on series voltage perturbation and shunt current perturbation and show that the former is better. (ii) We also show that the *dq* admittance can be identified efficiently by use of step response data instead of frequency scan. The former saves a great deal of time. (iii) For stability analysis, we examine the eigenvalues of the open-loop gain, the singular values, and the determinant of the return difference matrix. Results from those approaches provide cross-validation. Through *dq* admittance-based stability analysis, we have illustrated the impact of grid strength and solar irradiance on SSO. The methods reported in this paper can be readily adopted by system operators.

C. Paper Structure

The remainder of the paper is organized as follows. Section II describes the methods to obtain the *dq*-admittance frequency responses of IBRs via voltage or current perturbation, as well as sinusoidal perturbation or step perturbation. Section II also presents the passivity analysis results. Section III presents the stability analysis results. Section IV presents EMT simulation case studies to verify the stability analysis results. Finally, Section V summarizes the findings and concludes the paper.

II. *DQ* ADMITTANCE MODEL IDENTIFICATION

In the black-box EMT model for a bulk power system-connected solar PV provided by a vendor, the solar PV farm's circuit consists of a single grid-interconnected inverter, a dc-link capacitor, and the solar photovoltiaic source with solar irradiance as the input [14]. At its ac side, it is connected to a low-voltage bus and then a middle voltage bus at 20 kV through a transformer. The point of interconnection (POI) bus is at 66 kV. From the POI bus, the farm is connected to the transmission grid. An IBR is viewed at its POI and the frequency responses of its *dq*-admittance may be found via sinusoidal injection of either voltage perturbation or current perturbation. While the voltage perturbation is imposed at the POI as a series voltage injection, the current perturbation is imposed at the POI as a shunt current injection. In the following subsections, we present the two methods and the corresponding measurement results.

A. Shunt current injection

Here, we perturb the system with a small disturbance at the interface point. The injected current splits into converter i_m and grid current i_g, as illustrated in Fig. 1. All the perturbations are generated in the static *abc* frame.
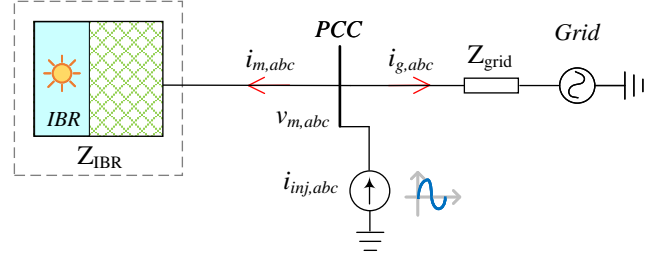

Fig. 1: *DQ*-admittance identification via shunt current injection.

For a three-phase ac system, the injected current is an amplitude-modulated three-phase signal and has the following expression in the *abc* static frame:

$$i_{\text{inj}_a} = I_m \cos(\omega_{\text{inj}}t)\cos(\omega_e t + \phi_{\text{inj}})$$

$$i_{\text{inj}_b} = I_m \cos(\omega_{\text{inj}}t)\cos(\omega_e t - \frac{2\pi}{3} + \phi_{\text{inj}}),$$

$$i_{\text{inj}_c} = I_m \cos(\omega_{\text{inj}}t)\cos(\omega_e t + \frac{2\pi}{3} + \phi_{\text{inj}}), \tag{1}$$

where ω_{inj}, ω_e, and ϕ_{inj} are the angular frequency of the injected current, system frequency, and phase angle of the injected current, respectively. For the sinusoidal function in (1), the space phasor is defined as :

$$\overrightarrow{i_{\text{inj}}}(t) = \frac{2}{3}\left[e^{j0}i_{\text{inj}_a}(t) + e^{j\frac{2\pi}{3}}i_{\text{inj}_b}(t) + e^{j\frac{-2\pi}{3}}i_{\text{inj}_c}(t)\right] \tag{2}$$

Substituting (1) in (2) we get:

$$\overrightarrow{i_{\text{inj}}}(t) = \frac{I_m}{2}e^{j\phi_{\text{inj}}}\left[e^{j(\omega_e+\omega_{\text{inj}})t} + e^{j(\omega_e-\omega_{\text{inj}})t}\right] \tag{3}$$

Also,

$$\overrightarrow{i_{\text{inj}}}(t) = (i_{\text{inj}_d} + ji_{\text{inj}_q})e^{j\omega_e t} \tag{4}$$

Thus, substituting for $\overrightarrow{i_{\text{inj}}}(t)$ in (3) and resolving $\overrightarrow{i_{\text{inj}}}(t)$ into the *d* and *q* axis components we get:

$$i_{\text{inj}_d} = I_m \cos(\omega_{\text{inj}}t)\cos(\phi_{\text{inj}}) \tag{5}$$

$$i_{\text{inj}_q} = I_m \cos(\omega_{\text{inj}}t)\sin(\phi_{\text{inj}}) \tag{6}$$

Three measurements, the converter current i_m, the grid current i_g and the PCC bus voltage v_m are recorded and they will be transformed from the *abc* frame into the *dq*-domain by applying the Park's transformation (7) with a transformation angle θ_s.

$$\begin{bmatrix} d \\ q \\ 0 \end{bmatrix} = \frac{2}{3} \begin{bmatrix} \cos(\theta_s) & \cos\left(\theta_s - \frac{2\pi}{3}\right) & \cos\left(\theta_s + \frac{2\pi}{3}\right) \\ -\sin(\theta_s) & -\sin\left(\theta_s - \frac{2\pi}{3}\right) & -\sin\left(\theta_s + \frac{2\pi}{3}\right) \\ 0.5 & 0.5 & 0.5 \end{bmatrix} \begin{bmatrix} a \\ b \\ c \end{bmatrix} \tag{7}$$

where $\theta_s = \omega_e t$, and $\omega_e = 2\pi \times 50$ rad/s. The inverse Park's transformation can be written as follows:

$$\begin{bmatrix} a \\ b \\ c \end{bmatrix} = \begin{bmatrix} \cos(\theta_s) & -\sin(\theta_s) & 1 \\ \cos\left(\theta_s - \frac{2\pi}{3}\right) & -\sin\left(\theta_s - \frac{2\pi}{3}\right) & 1 \\ \cos\left(\theta_s + \frac{2\pi}{3}\right) & -\sin\left(\theta_s + \frac{2\pi}{3}\right) & 1 \end{bmatrix} \begin{bmatrix} d \\ q \\ 0 \end{bmatrix} \tag{8}$$

The dq-frame should be aligned with the the PCC bus voltage's space vector. Most of the papers achieve this alignment through a PLL. However, the noise in the measurement data due to the perturbation and the PLL bandwidth can affect the alignment, leading to inaccurate admittance measurement [15] and [16]. In this paper, we are able align the synchronous dq-frame with the PCC bus voltage space vector exactly since the grid voltage adopted in the measurement testbed is a voltage source with synchronous frequency.

Fast Fourier Transform (FFT) is then applied to extract the phasor components of the measured dq-voltages and currents. The measured current and voltage are related by the IBR's impedance matrix evaluated at the injection frequency, as shown in (9).

$$\begin{bmatrix} v_{m_{d1}}(f_{\text{inj}}) \\ v_{m_{q1}}(f_{\text{inj}}) \end{bmatrix} = \underbrace{\begin{bmatrix} Z_{dd}(f_{\text{inj}}) & Z_{dq}(f_{\text{inj}}) \\ Z_{qd}(f_{\text{inj}}) & Z_{qq}(f_{\text{inj}}) \end{bmatrix}}_{\mathbf{Z}_{dq}} \begin{bmatrix} i_{m_{d1}}(f_{\text{inj}}) \\ i_{m_{q1}}(f_{\text{inj}}) \end{bmatrix} \quad (9)$$

where $f_{\text{inj}} = \omega_{\text{inj}}/(2\pi)$. dq-impedance is a 2×2 matrix, and (9) is under-determined since it consists of four unknowns and only two sets of equations. Therefore, two sets of linearly independent measurements are required to solve (9). Hence, we inject another set of currents at the same frequency but with a different phase angle ϕ_{inj_2}. This methodology has been previously discussed in [17] and [18].

$$\begin{bmatrix} v_{m_{d2}}(f_{\text{inj}}) \\ v_{m_{q2}}(f_{\text{inj}}) \end{bmatrix} = \underbrace{\begin{bmatrix} Z_{dd}(f_{\text{inj}}) & Z_{dq}(f_{\text{inj}}) \\ Z_{qd}(f_{\text{inj}}) & Z_{qq}(f_{\text{inj}}) \end{bmatrix}}_{\mathbf{Z}_{dq}} \begin{bmatrix} i_{m_{d2}}(f_{\text{inj}}) \\ i_{m_{q2}}(f_{\text{inj}}) \end{bmatrix} \quad (10)$$

Combining (9) and (10), we can find the impedance at f_{inj}:

$$\mathbf{Z}_{dq} = \begin{bmatrix} v_{m_{d1}}(f_{\text{inj}}) & v_{m_{d2}}(f_{\text{inj}}) \\ v_{m_{q1}}(f_{\text{inj}}) & v_{m_{q2}}(f_{\text{inj}}) \end{bmatrix} \begin{bmatrix} i_{m_{d1}}(f_{\text{inj}}) & i_{m_{d2}}(f_{\text{inj}}) \\ i_{m_{q1}}(f_{\text{inj}}) & i_{m_{q2}}(f_{\text{inj}}) \end{bmatrix}^{-1} \quad (11)$$

The subscripts 1 and 2 refer to measurements during two independent injections. Finally, we can obtain the dq-admittance of the inverter by taking the inverse of (11). The measured dq-admittance can be viewed as a multi-input, multi-output linearized model of the inverter about an operating point in the frequency domain.

a) Challenges in current injection-based measuring method: The foremost challenge is the sophistication of the measurement testbed. To have a grid-following converter function, a voltage source has to be provided. Additionally, the shunt current injection testbed requires a shunt current source.

Secondly, in order to precisely identify the system through shunt current injection, we must inject a current signal with a magnitude sufficient large to measure the response. Simultaneously, we should ensure no significant deviation in the steady-state operating condition. Here, I_m has to be chosen to have greater than 5% of the nominal value.

The third challenge is related to the numerical computation which is presented in (11). It can be seen that compared to the other method, computing requires matrix inverse which requires that the matrix be nonsingular. Therefore, additional checks on singularity is required and it is possible singularity occurs when the system has undamped oscillations. Fig. 2a
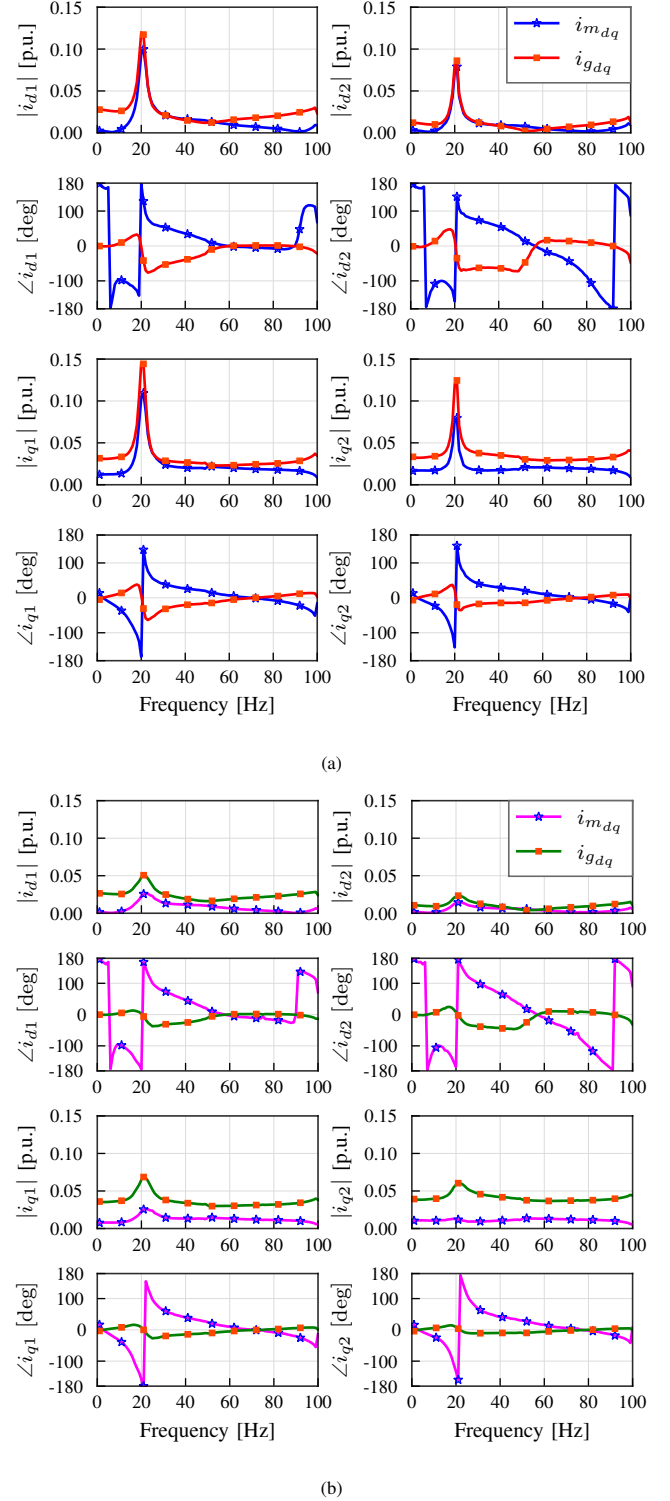

Fig. 2: (a) Measured current phasors at the converter and grid terminal, when SCR = 5. (b) Measured current phasors at the converter and grid terminal when the SCR= 10.

presents the measured current injected at the inverter (i_m) and grid (i_g) terminal, when the SCR = 5. We observe a steep peak in the grid and converter current around 20 Hz, and the magnitude of the measured current is greater than the injected current, indicating a possible resonance condition.

When the measurements have resonances, the matrix used for inverse in (11) will experience singularity. This leads to inaccurate computation and the resulting inverter admittance measurements are inaccurate.

We performed the current injection with grid SCR = 10 to resolve the issue, and we observed the magnitude of the measured current at the converter is almost similar across the 1-100 Hz frequency range, reflecting no large deviation from the steady state operating condition, as shown in Fig. 2b. Note, for both the grid conditions, the injection point and the magnitude (0.05 p.u.) of the disturbance injected are the same.

The resulting converter and grid impedance is presented in Fig. 3. Fig. 3b presents the measured grid impedance for two different SCRs (5 and 10). The grid is modeled as an infinite voltage source behind an RL circuit, and we do not observe any difference between the measured and analytically derived impedance. Fig. 3a compares the measured inverter impedance when the grid SCR is 5 or 10. We observe discrepancy in components in low frequency and around 20 Hz. The impedance results measured under SCR =5 should not be used since they may lead to inaccurate stability analysis. Thus, for the shunt current injection method, the challenge is not only selecting the appropriate current magnitude but also making sure the system does not have poorly damped oscillation modes.

B. Series voltage injection

To measure the frequency response of the IBR through series voltage injection, we connect an ideal voltage source at the PCC bus. We have ensured the system reflects the online operating condition during the measurement by setting the *dq* axis voltage as shown in Fig. 4. A sinusoidal signal of 0.1 p.u. peak-to-peak amplitude is superimposed on the *d* and *q* axis voltages. The *d*-axis of the *dq*-frame is aligned with the PCC voltage vector.

Here, we identify the *dq* -admittance by applying a sinusoidal perturbation to the voltage in *dq* frame around the steady-state operating condition, as shown in Fig. 4. Note the *d* and *q* axes are perturbed separately at all desired frequencies. We have assumed the measured current to be flowing into the inverter, and the *dq* -admittance is represented as:

$$Y_{dd}(f_{\text{inj}}) = \frac{i_d^{(1)}(f_{\text{inj}})}{v_d^{(1)}(f_{\text{inj}})}, \ \ Y_{dq}(f_{\text{inj}}) = \frac{i_d^{(2)}(f_{\text{inj}})}{v_q^{(2)}(f_{inj})}$$

$$(12)$$

$$Y_{qd}(f_{\text{inj}}) = \frac{i_q^{(1)}(f_{\text{inj}})}{v_d^{(1)}(f_{\text{inj}})}, \ \ Y_{qq}(f_{\text{inj}}) = \frac{i_q^{(2)}(f_{\text{inj}})}{v_q^{(2)}(f_{\text{inj}})},$$

where superscripts (1) and (2) refer to perturbations in the *d* and *q* axes, respectively; $f_{inj} = \begin{bmatrix} f_1, f_2, \dots f_n \end{bmatrix}$ are the frequencies at which the system is perturbed.

The measured three-phase current vector $\begin{bmatrix} i_a, i_b, i_c \end{bmatrix}^T$ is translated from *abc* frame to *dq*-frame by the Park's transformation. The phasor components of the *dq* voltage and current components at each injected frequency are computed by applying the FFT analysis.
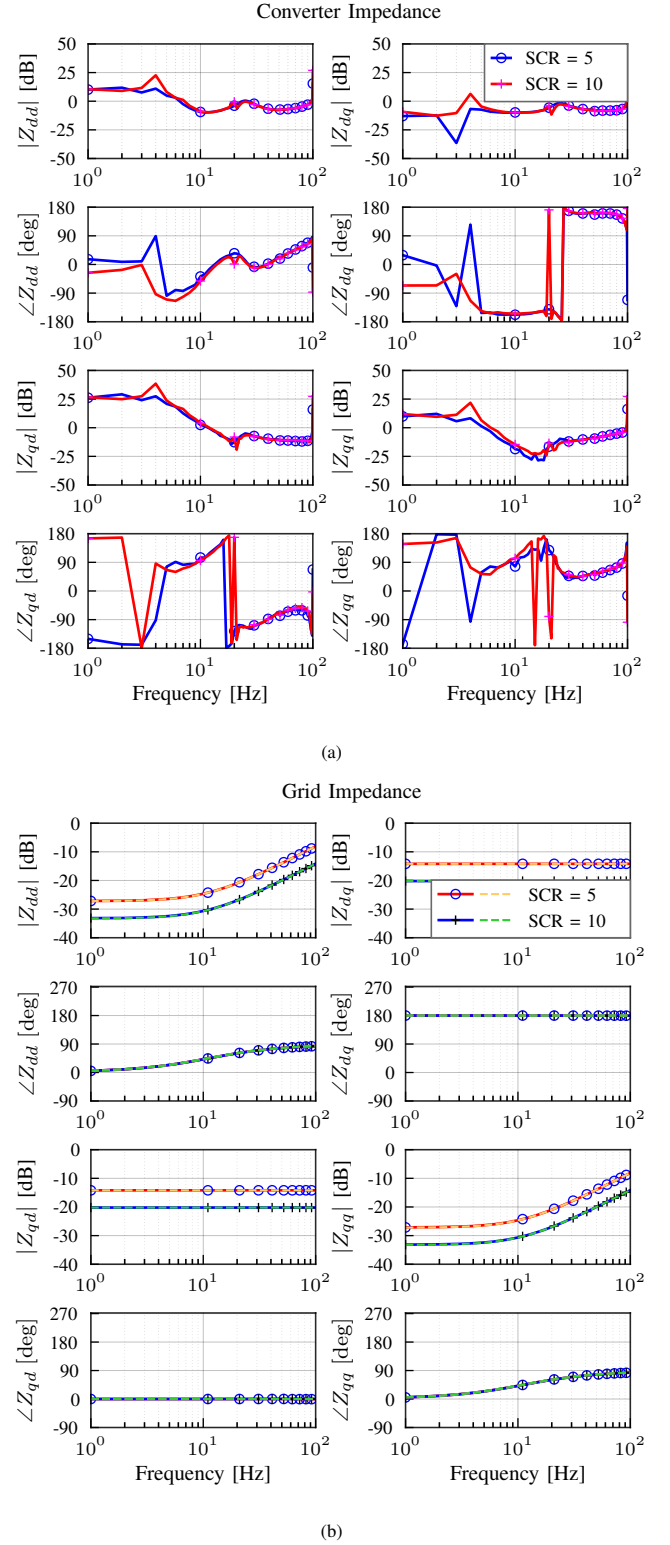

(a)

(b)

Fig. 3: *dq*-impedance of the PV plant and grid obtained via Current Injection for two different grid conditions (a) Converter impedance when the grid short circuit ratio is 5 and 10. (b) Grid impedance when the SCR = 5 and 10, dotted line: Analytical, line with a marker: measured impedance.

The foremost challenge is recording appropriate measurements for identifying small-signal admittance. Fig. 5 shows an example. At $t = 15$ s, a 0.05 p.u. voltage is injected at the 66-kV voltage level. The responses of the system for 30
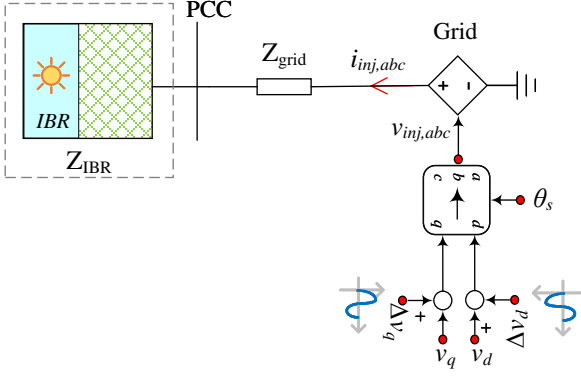
Fig. 4: *dq*-admittance identification via series voltage injection.

Hz and 100 Hz perturbation are different, as shown in Fig. 5. The system takes a relatively long time to settle down when injected with a 100-Hz sinusoidal signal. We use the steady-state data for FFT. Hence, the data from 17 s-18 s are used for FFT.
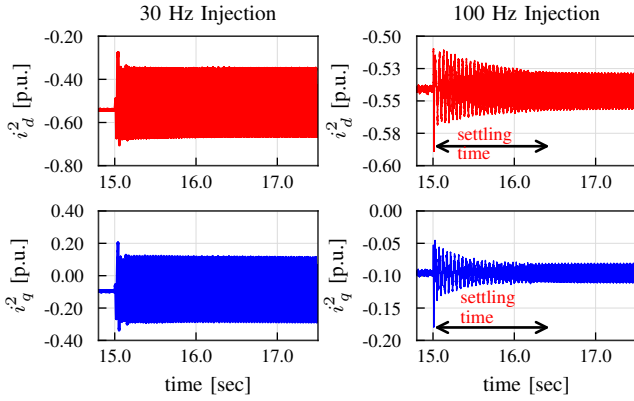

Fig. 5: *dq* current measurements recorded when the *q*-axis voltage is perturbed.

C. Admittance identification results

We extract the *dq* admittance frequency responses from the detailed EMT simulation model through frequency scan. Fig. 6 presents a comparison between the voltage and current injection. For both injection techniques, the measurement and injection point are similar, as shown in Fig. 1 and Fig. 4. The results agree with each other.

On the other hand, from the above experiments, we find that the series voltage injection method is more appealing since only a smaller magnitude of disturbance is applied, while for shunt current inject, a greater disturbance has to be applied to the system.

To illustrate that the small-signal admittance model is a function of the steady-state operating condition, we have identified the admittance for three irradiation levels. For instance, when the irradiance is 200 W/m^2 and 300 W/m^2, the magnitude of Y_{dd} at 0 Hz corresponds to 0.34 p.u. and 0.56 p.u., as shown in Fig. 7.
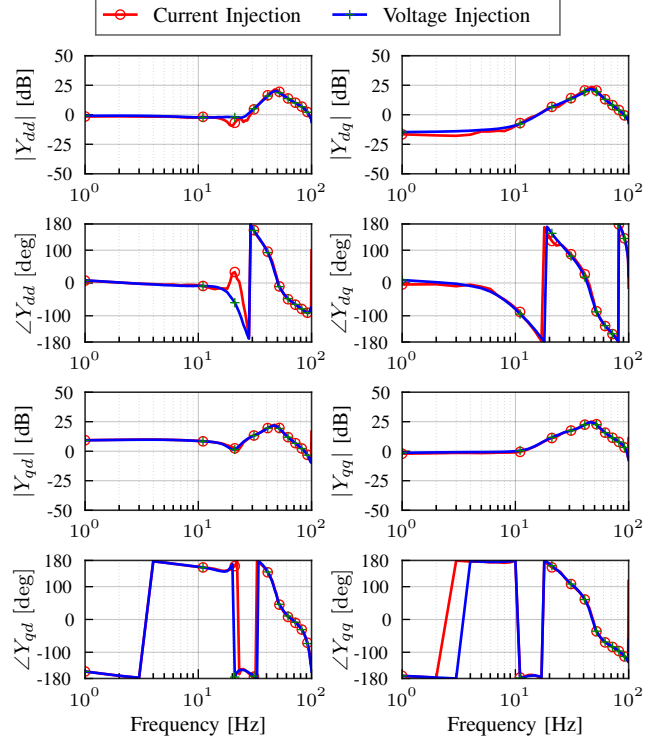

Fig. 6: *dq* admittance of the PV plant obtained via voltage and current injection when the sun irradiance is 300 W/m^2
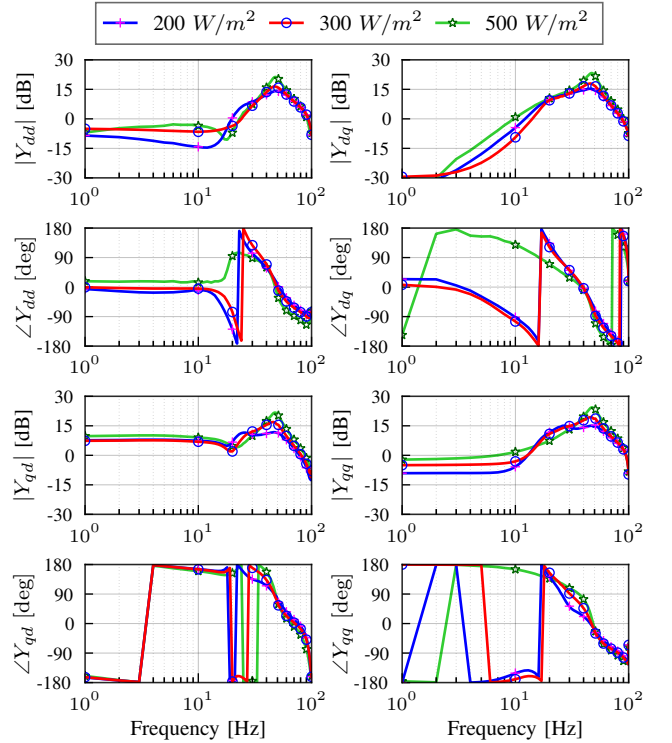

Fig. 7: *dq* admittance of the PV plant identified via voltage injection when the irradiance = 500 W/m^2, 300 W/m^2. and 200 W/m^2.

To further validate these observations, we have conducted *dq*-admittance-based analysis using the Generalized Nyquist
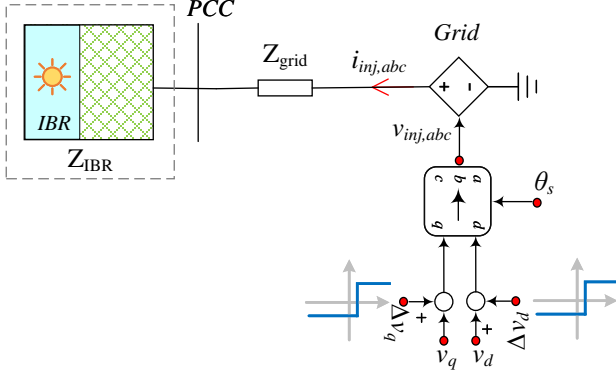
criterion and EMT simulations.

Fig. 8: The measurement testbed for dq admittance identification via step injection.

D. Step Injection

Here, we estimate $\mathbf{Y(s)}$ the MIMO transfer function of the system by using the time-domain dq-axis current measurements upon step injection in the dq voltage source.

$$\mathbf{Y}(s) = \begin{bmatrix} Y_{dd}(s) & Y_{dq}(s) \\ Y_{qd}(s) & Y_{qq}(s) \end{bmatrix} \quad (13)$$

In this method, we require only two perturbations to estimate the dq-admittance of the system, $\mathbf{Y(s)}$. All the perturbations are initially applied in the dq-domain and then transformed to the abc domain by applying Park transformation (7). We apply a step change to the grid voltage in dq-domain and measure the three-phase currents at the grid, as shown in Fig. 8. The measured currents are then transformed to the dq-domain by applying the inverse-Park transformation (8). For the d-axis voltage perturbations we get $i_d^{(1)}(t)$ and $i_q^{(1)}(t)$ through which we can estimate $Y_{dd}(s)$ and $Y_{qd}(s)$ as follows.

$$Y_{dd}(s) = \frac{i_d^{(1)}(s)}{v_d^{(1)}(s)}, \ Y_{qd}(s) = \frac{i_q^{(1)}(s)}{v_d^{(1)}(s)}. \quad (14)$$

Similarly through the q-axis voltage injection we measure $i_d^{(2)}(t)$ and $i_q^{(2)}(t)$ to identify $Y_{dq}(s)$ and $Y_{qq}(s)$ as follows:

$$Y_{dq}(s) = \frac{i_d^{(2)}(s)}{v_q^{(2)}(s)}, \ Y_{qq}(s) = \frac{i_q^{(2)}(s)}{v_q^{(2)}(s)}. \quad (15)$$

The superscripts (1) and (2) in 14 and 15 refer to d-axis and q-axis voltage perturbations, respectively. From the measured output and input data, we estimate the transfer function $Y_{dd}(s)$, $Y_{qd}(s)$, $Y_{qd}(s)$ and $Y_{qq}(s)$ by using the transfer function estimation algorithm, `tfest` [19].

To generate the continuous time input-output signal, we apply a 0.025 p.u. step change to the d- or q-axis voltage separately, and the step responses of the dq current measurements are shown in Fig. 9. The recorded measurements in Fig. 9 have a sampling rate of 20 kHz. The measurements are noisy since we have used a high-fidelity EMT model. The accuracy of the estimated model depends on the input data

to the algorithm. Hence, we have adopted the following data pre-processing techniques:

- To better estimate the system, we reduce the noise in the measured output data using MATLAB's smooth data function. Note that we need to select an optimum window size so that the smooth data accurately represents the actual measurement. In Fig. 10, we have reduced the noise by selecting a window size of 100 data points and using the moving average method.
- The `tfest` algorithm also works best with zero-mean time-series data. Therefore, we subtract the steady-state dc offset from the input and output signal.

The model estimation and order selection process is iterative. First, we assume a low model order and load the time-domain data to obtain the initial estimate of the model. During validation, we compare the simulated time response of the estimated model to the measured output, as shown in Fig. 11. The normalized root mean square (NRMSE) is used as an index to measure the fit between the simulated response of the estimated system and the measured output data. This value is shown in the legend of the simulated response comparison plots Fig. 11.

If we do not observe a good fit, we can increase the model order incrementally. Note that the model order should be the same for all the estimated models. We can also change the resolution and time duration of the input data used for identification to get a better fit. Fig. 11 shows the simulated response comparison for a 6th-order approximation of the system. The simulated response is comparable to the measured data with an excellent fit.

Finally, to validate the efficacy of the step-injection method, we compare the frequency response of the estimated model to the dq-admittance model obtained through frequency scan. Fig.12 shows that the dq-admittance models obtained by both methods are identical.

Remarks: Frequency scan is very time-consuming, especially given that the power electronic switching dynamics are included in the black-box model. In contrast, step injection is a rapid system identification technique requiring only two-step perturbations.

E. Passivity Check

Generally, a system is passive if it can dissipate active power at all frequencies. The input admittance should have non-negative conductance at any frequency for an inverter to be passive [20]. The input dq-admittance of the IBR is passive if the eigenvalues of the sum of the admittance and its Hermitian are positive [21], [22]:

$$\lambda\left(Y(j\omega) + Y^H(j\omega)\right) > 0 \quad \forall\omega \quad (16)$$

where λ is the eigenvalue of $Y(j\omega) + Y^H(j\omega)$, and $Y^H(j\omega)$ is the Hermitian or the conjugate transpose of $Y(j\omega)$. If one of the eigenvalues $\lambda_{1,2}$ is negative, this indicates the dq admittance is non-passive and may lead to potential oscillation issues at the evaluated frequency.

Fig. 13 shows the eigenvalues of $Y(j\omega) + Y^H(j\omega)$ for different irradiation conditions. The eigenvalue λ_1 is positive
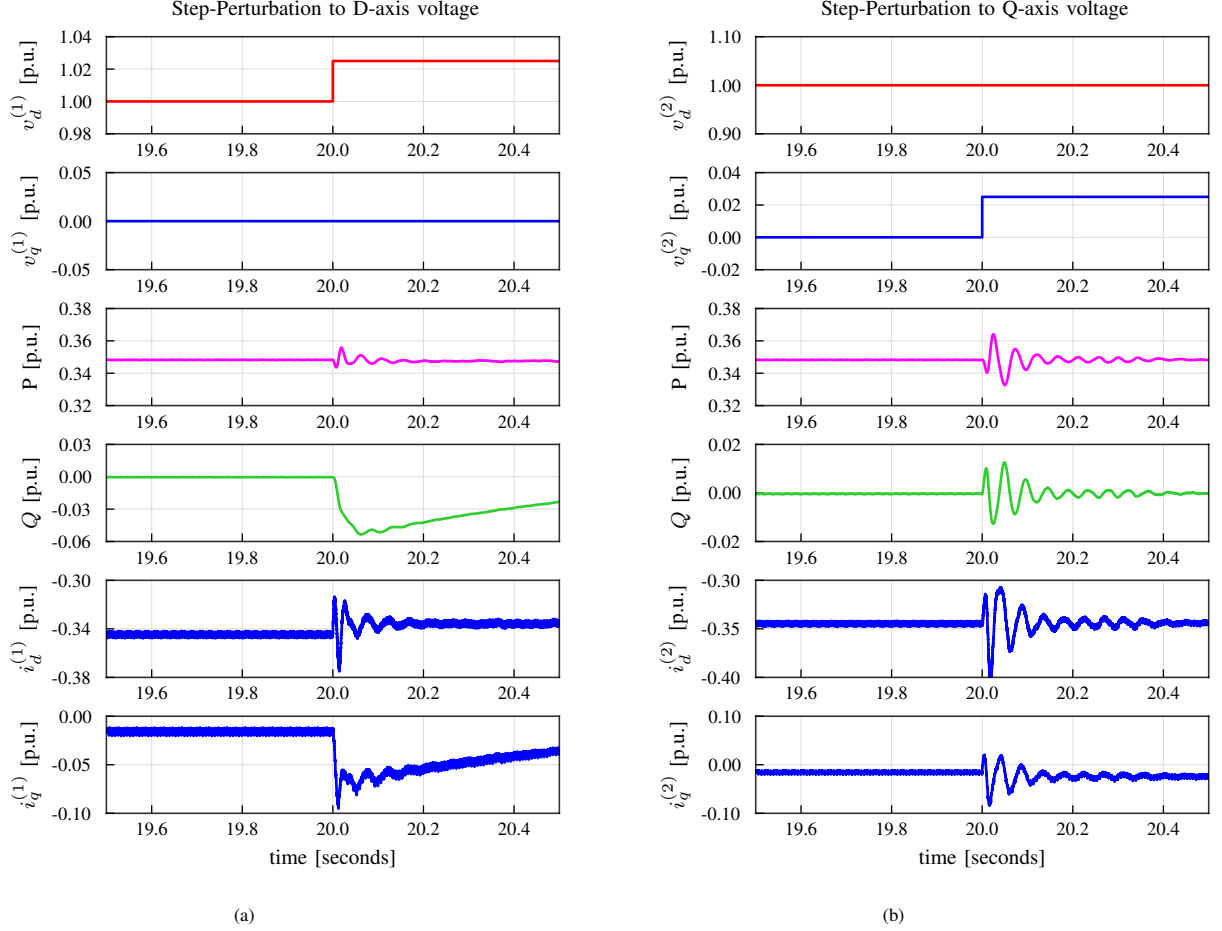
Fig. 9: Step responses of the system for a 0.025-p.u. step change in the *d*- and *q*-axis of the grid voltage. Irradiation level at the time of perturbation is 200 W/m^2.

for all frequencies. However, the eigenvalue λ_2 is negative between 0 Hz -40 Hz for all irradiation. Thus, the system is non-passive, with a high probability of sub-synchronous oscillations. The eigenvalue λ_2 is the lowest for irradiation 200 W/m^2 at the region of 10 Hz to 25 Hz. Hence we can infer that a decrease in irradiation level negatively affects the passivity of an IBR. We will apply the Generalized Nyquist criterion to further investigate the interaction between the IBR and grid in the following sections.

III. *DQ*-ADMITTANCE BASED STABILITY ANALYSIS

DQ-admittance-based stability analysis offers an effective method to analyze the small-signal stability of power electronic devices when detailed internal information of the system is not publicly accessible. In this method, the Generalized Nyquist criterion (GNC) is applied to evaluate the stability of power-electronic systems at the interconnection.

GNC [23] states that the system is stable if and only if the eigenvalue loci of the open loop gain, $L(s)$ do not encircle the point (-1, j0) in the 2D plane. The GNC is valid only under the assumption that both Y_{conv} and Z_g are stable, i.e., the IBR operates stably when connected to a stiff voltage source and the grid is stable. These two conditions are true for the practical scenario.

Fig. 14 shows a grid-integrated IBR. The IBR can be viewed as a Norton circuit, a current source parallel to an admittance $Y_{\text{conv}}(s)$. The grid is represented by a Thévenin equivalent and has a source impedance $Z_g(s)$. The impedance/admittance can be viewed in a static frame or the *dq*-frame. For the circuit in Fig. 14, the current can be solved using the following equation:

$$i(s) = (I + Y_{\text{conv}}Z_g)^{-1}(Y_{\text{conv}}v_g(s) - i_c(s)) \qquad (17)$$

If we consider current as the output y and $(Y_{conv}v_g(s) - i_c(s))$ as the input u, the circuit can be viewed as a feedback system, as shown in Fig. 14. The open-loop gain is defined as :

$$L(s) = Y_{\text{conv}}(s)Z_g(s) \qquad (18)$$

where $Y_{\text{conv}}(s)$ is the measured *dq*-admittance of the converter, and $Z_g(s)$ is the *dq*-impedance of the grid. In general, the grid impedance is represented as:

$$Z_{g\,dq}(s) = \begin{bmatrix} R_g + sL_g & -\omega_e L_g \\ \omega_e L_g & R_g + sL_g \end{bmatrix} \qquad (19)$$

The grid impedance and inverter admittance are 2×2 matrices in the *dq*-domain. Consequently, the open-loop gain,
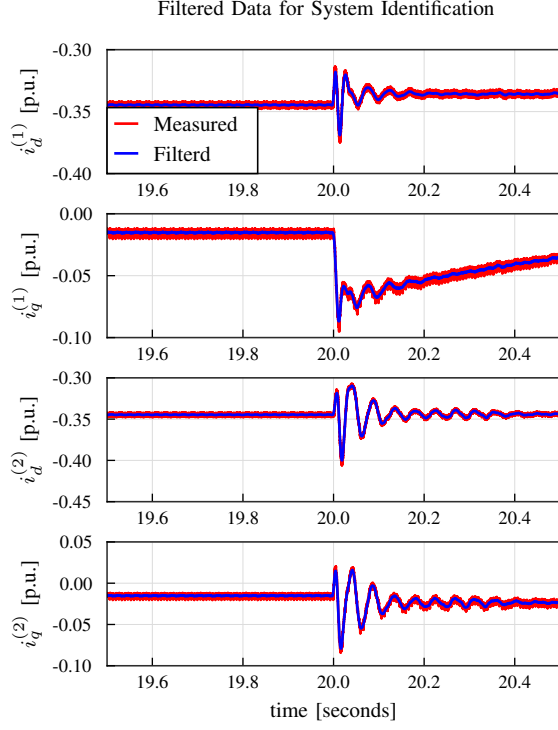
Fig. 10: Comparison of noisy measured output data and smooth output data.
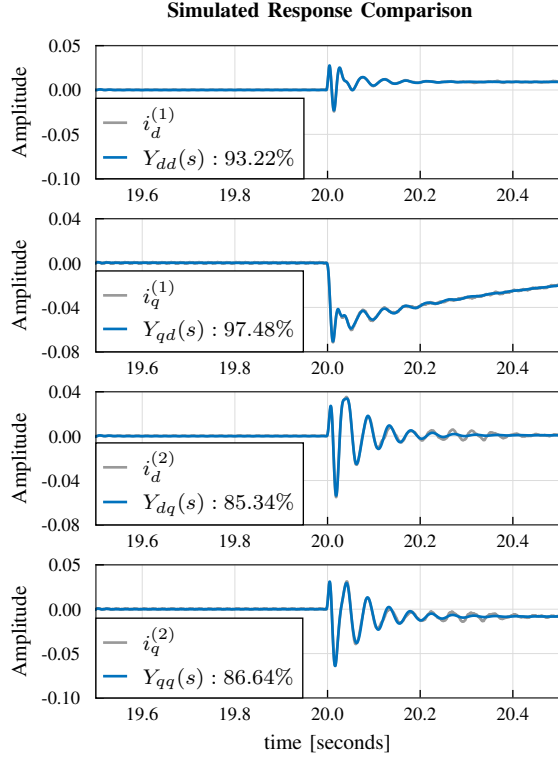

Fig. 11: Comparison of the measured output data and the simulated response of the estimated dq-admittances.

$L(s)$ will have two eigenvalues $\lambda_1(s)$ and $\lambda_2(s)$.

$$\begin{bmatrix} \lambda_1(s) \\ \lambda_2(s) \end{bmatrix} = \text{eig}\,(L(s)). \qquad (20)$$
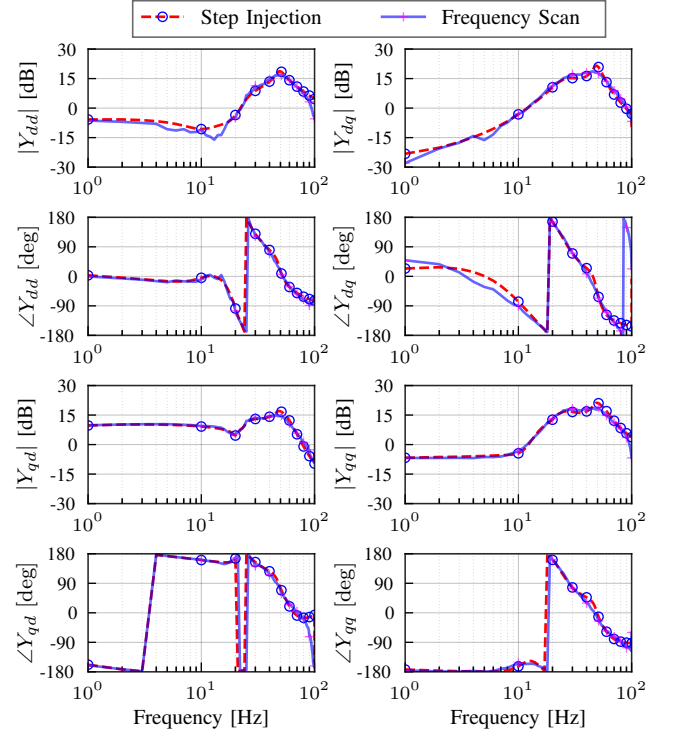

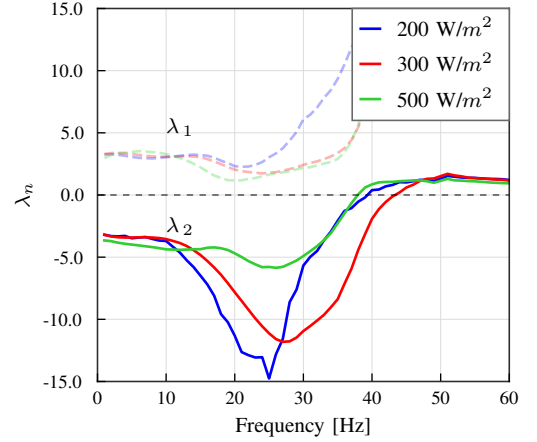Fig. 12: dq admittance of the PV plant obtained via step injection and frequency scan when the sun irradiance is 200 W/m^2.

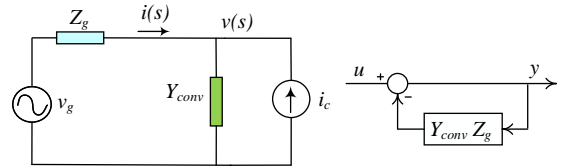Fig. 13: Eigenvalues plot of $Y(j\omega) + Y^H(j\omega)$ for different irradiation conditions.

Fig. 14: Circuit representation of the grid-integrated IBR and the corresponding feedback system.
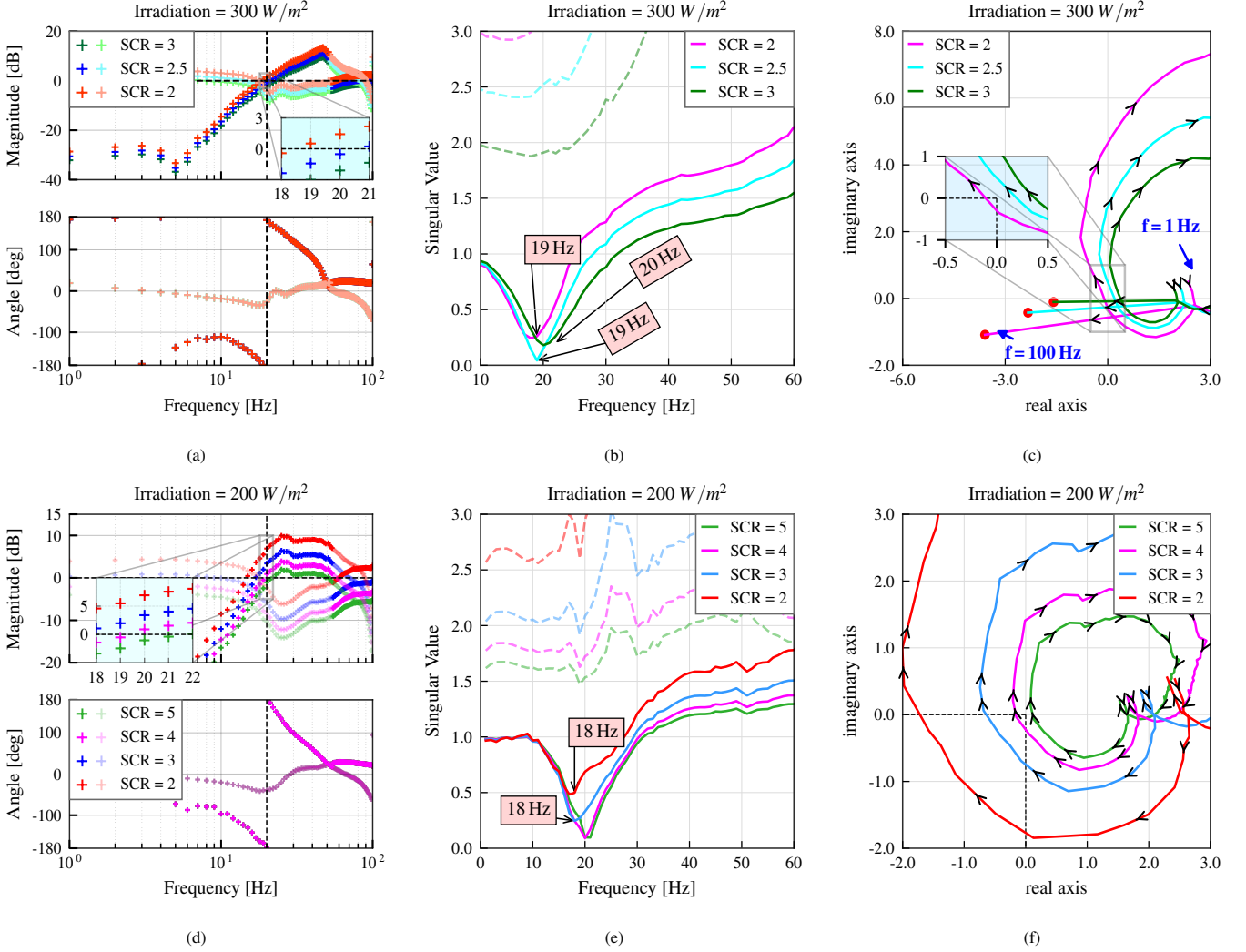
Fig. 15: (a)(b)(c) Irradiance at 300 W/m^2 (a) Bode plot of the eigenvalues of $(Y_{\text{conv}}(s)Z_g(s))$, phase-shift at 19 Hz (b) Singular value plot of $(I + Y_{\text{conv}}(s)Z_g(s))$ (c) Nyquist plot of $\det(1 + Y_{\text{conv}}(s)Z_g(s))$. (d)(e)(f) Irradiance at 200 W/m^2. (d) Bode plot of the open-loop gain's eigenvalues. (e) Singular value plot of $(I + Y_{\text{conv}}(s)Z_g(s))$ (f) Nyquist plot of $\det(1 + Y_{\text{conv}}(s)Z_g(s)$.

A. Stability evaluation criteria

In *dq*-admittance-based stability analysis, the usual method to determine the closed-loop stability of the system is to apply the GNC to the open-loop gain. This approach has been adopted by [12], [23], [24]. Since the open-loop gain is a 2×2 matrix, its eigenvalue loci are used as two SISO systems' loop gains for stability check. Additionally, we can examine the return difference matrix [25]. This method was adopted in [26] to evaluate type-3 wind farm subsynchronous resonance stability. As a total, we may generate three types of plots for stability check, including Bode plots for the open-loop gain eigenvalue loci, singular values of the return difference matrix, and the Nyquist plot of the determinant of the return difference matrix.

For the feedback system in Fig. 14, since the open-loop gain is $L(s) = Y_{\text{conv}}Z_g$, we can see that the closed-loop transfer function from u to the error $e = u - y$ is as follows:

$$\frac{e(s)}{u(s)} = (I + L(s))^{-1}. \tag{21}$$

$I + L(s)$ is the return difference matrix and the closed-loop system's eigenvalues are the roots of the determinant of the return difference matrix. Therefore, the determinant's frequency response may be used for stability check.

- Determinant-based stability criterion: If the determinant of the return difference matrix $(1+L(s))$ does not encircle the origin $(0, j0)$ clockwise, then the system is stable [27].

$$\det(I + L(s)) = \prod_{i=1\ldots n} (s - \lambda_{\text{cl},i}) \tag{22}$$

where $\lambda_{\text{cl},i}$ are the closed-loop system's eigenvalues. The sufficient and necessary condition for all eigenvalues to be located in the left half-plane is to have the determinant not encircle the origin.

- Singular values of the return difference matrix: When the return difference matrix $I + L(s)$ is evaluated at a frequency $s = j\omega$, if the matrix becomes singular, this indicates that $s \approx j\omega$ is a root of the matrix's determinant. At this frequency, the determinant becomes 0, or the matrix becomes singular. Since the singular values of the

matrix can imply singularity, the singular values over the frequency domain can indicate at which frequency the system may experience instability. In other words, the singular values can show the oscillation frequency. Singular value plots can be used along with the determinant-based Nyquist plot to examine whether the system is stable and what the oscillation frequency is.

- Bode stability criterion: If the eigenvalue loci of $L(s)$ have a gain less than 0 dB at the frequency of phase shifting (from $-180°$ to $+180°$), or a phase greater than $-180°$ when the gain is 0 dB, then the system is stable. Otherwise, it is unstable [24].

B. Case studies

To predict SSOs, we have conducted *dq*-admittance-based stability analysis. The effect of irradiance and system strength on SSOs are reported in the following sub-sections.

We have evaluated the interaction between the PV system dynamics and the grid for two irradiation levels, 200 W/m² and 300 W/m².

a) Irradiation $300W/m^2$*:* Fig. 15a presents the Bode plot of the open-loop gain, $Y_{\text{conv}}(s)Z_g(s)$ from 1 to 100 Hz, for different SCRs when irradiation is 300 W/m². We observe a phase shift from $-180°$ to $180°$ in the eigenvalue locus of $\lambda_1(s)$ at 19 Hz for SCR = 3, 2.5 and 2. For SCR = 2, the open-loop gain magnitude (0.5 dB) is greater than 0 dB, and the determinant loci of the return difference matrix $(I + Y_{conv}(s)Z_g(s))$ encircles $(0, j0)$ in a clockwise direction, as seen in Fig. 15c. This indicates the system will become unstable when SCR is less than 2.

Fig. 15b shows that the return difference matrix has a singular value less than 0.5 from 13 Hz to 23 Hz. However, it is near zero, around 18 Hz to 20 Hz. For SCR = 2, Fig. 15b indicates the system might have an SSO around 19 Hz. Further, the oscillation frequency for SCR = 3 and SCR = 2.5 are 19 and 20 Hz, respectively.

Fig. 15c shows the Nyquist plot of the determinant of the return difference matrix. We do not observe any clockwise encirclement of $(0, j0)$ when SCR is 2.5 or 3. When SCR is 2, the determinant loci encircle the origin. This indicates instability.

Therefore, both the Bode plot of the open-loop gain's eigenvalue loci and the Nyquist plot of the determinant of the return difference matrix implicate that the system is unstable when SCR is less than 2. Furthermore, the Bode plot and the singular value plot indicate that the oscillation frequency is 19 Hz.

b) Irradiation 200 *W/m²:* Fig. 15d presents the Bode plot of the open loop gain $Y_{\text{conv}}(s)Z_g(s)$ for different grid strengths. A phase shift from $-180°$ to $180°$ happens at 20 Hz. For SCR = 5, 4, 3, and 2, the open-loop gain of $L(s)$ at 20 Hz is -1.04 dB, 0.88 dB, 3.39 dB, and 6.91 dB, respectively. This indicates that when the grid SCR is ≤ 4, the PV system is unstable since the magnitude of the loop gain is greater than 0 dB at the phase shifting frequency. The frequency when phase shifts is 20 Hz, implicating the oscillation frequency is 20 Hz.

Based on the Nyquist plot of the determinant of the return difference matrix in Fig. 15f, we can evaluate the performance

of the inverter when irradiation is 200 W/m². For SCR ≤ 4, the determinant encircles the point $(0, j0)$ in the clockwise direction. Hence, the system is unstable when the SCR is reduced beyond this value.

Further, we can discern the frequency of the SSO from the singular value plot (Fig. 15e) of the return difference matrix. When the SCR = 2 and 3, the singular value is minimum at 18 Hz, indicating a potential SSO around that frequency. When the SCR = 4 and 5, there is a dip in the singular value around 20 Hz. From the above observations, we can infer that the oscillation frequency varies with the grid strength.

For the 200 W/m² irradiance scenario, we again see that methods based on the open-loop gain or the return difference matrix lead to the same stability analysis results.

Comparing the two irradiance scenarios, we find that at the lower irradiance condition, the system is more prone to weak grid instability which manifests as SSOs at 18 Hz-20 Hz.

IV. EMT SIMULATION RESULTS

To verify the effectiveness of the *dq*-admittance-based analysis methods, we have conducted EMT simulations on the detailed switch model in the PSCAD/EMTDC software environment. The following subsections provide the results of the case studies.

### A. Change in irradiance from 500 W/m² to 300 W/m²

Here, the dynamic performance of the PV system in weak grids is evaluated by varying the solar irradiation level.

Initially, the irradiance and the power order are set to 500 W/m² and 66 MW, respectively. The system delivers 0.66 p.u. real power (based on 100 MW power base) and zero reactive power. The PV is operating at 1.02 pu terminal voltage. At t = 15 s, the irradiance is stepped down from 500 W/m² to 300 W/m². Fig. 16a shows the system's response when the grid's SCR is 3, 2.5, and 2 respectively. The system is stable when SCR is 3. The inverter delivers 0.56 p.u. real power and the system reaches steady-state condition quickly. When SCR is 2, we observe SSO in the RMS voltage measurement, real and reactive power. These observations are consistent with the *dq*-admittance-based analysis.

FFT analysis of the RMS voltage indicates the system is oscillating around 19 Hz, Fig. 16b. These findings verify the SSO frequency predicted through the singular value plot, Fig. 15b.

Furthermore, we also observe a second harmonic component of the oscillation frequency at 38 Hz, as shown in Fig. 16b. This harmonic component is generated by nonlinear interaction due to phase modulation as explained in [28]. Briefly, if the system has an oscillation at $f = 19Hz$, then the output phase angle from the phase-locked-loop in IBR (relative to the synchronized dq frame) δ has 19 Hz oscillations ($\delta = \delta_0 + \beta \sin(2\pi f t)$). Consequently, the voltage phasor observed in the synchronized frame has the following expressions:

$$\overline{V} = \hat{v}e^{j\delta} = \hat{v}e^{j\delta_0}e^{j\beta \sin(2\pi f t)}$$

$$= \hat{v}e^{j\delta_0} \sum_{n=-\infty}^{\infty} J_n(\beta)e^{j2\pi n f t}. \tag{23}$$
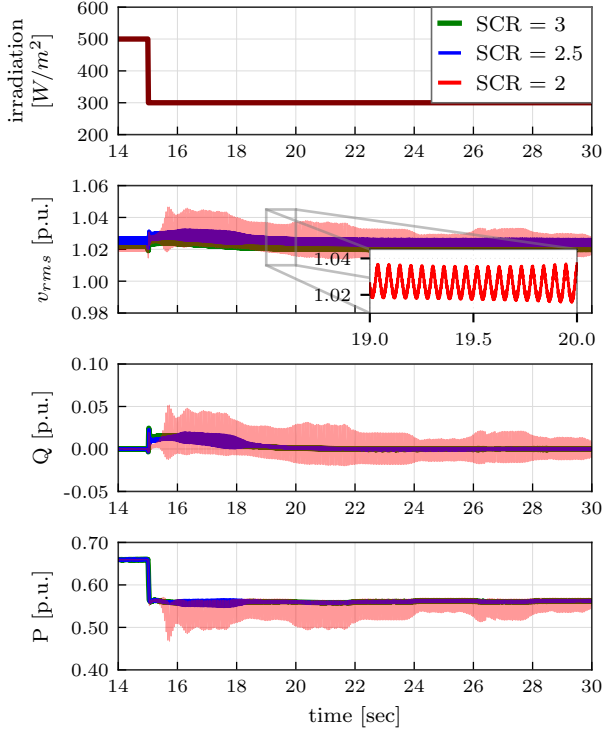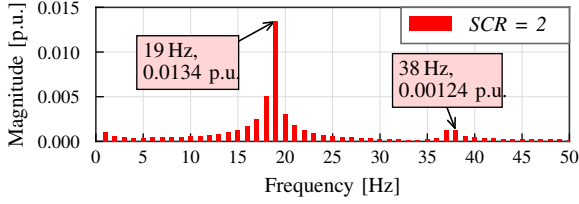
Fig. 16: (a) Dynamic response of the inverter when the irradiation is stepped down from 500 W/m^2 to 300 W/m^2, (b) FFT analysis results of the RMS voltage measurements shown in Fig. 16a.

where $J_n(\beta)$ is the Bessel function. It can be seen that the dq voltage signal is subjected to phase modulation and phase modulation generates harmonics. In this case, it can be seen that

$$\frac{J_2(\beta)}{J_1(\beta)} = \frac{0.00124}{0.0134} = 0.0925. \qquad (24)$$

The estimated value of β is 0.36 radian or 20°.

B. Line-tripping event

In order to validate the analysis result, we evaluate the IBR's dynamic performance following the loss of the transmission line using EMT simulations. Fig. 15d and 15e suggest that SSO occurs in the system when irradiance is 200 W/m^2 and the grid's SCR is less than 4.

Initially, the system is stable for irradiation 200 W/m^2 and SCR at 5. The inverter delivers 0.34 p.u. of real power to the grid. At $t = 15$ s, we have simulated a large disturbance by tripping one of the 66 kV transmission lines. This leads to a
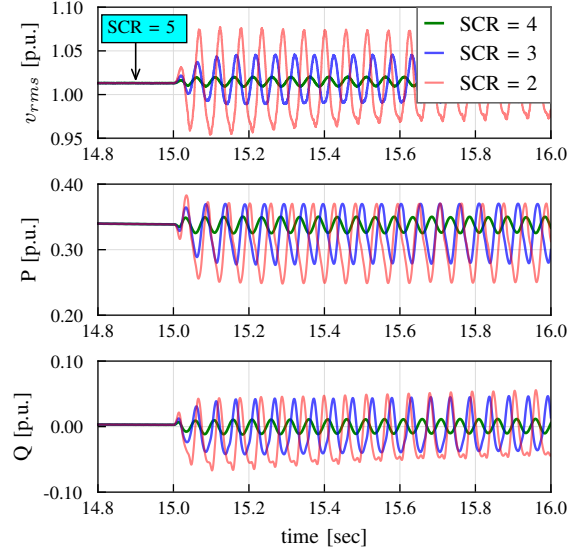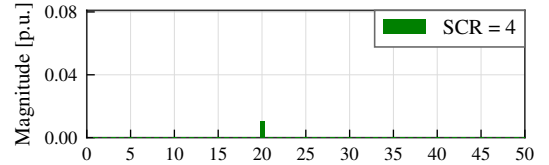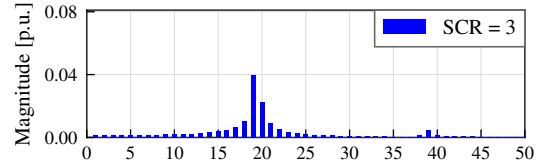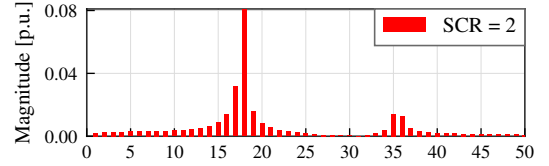
Fig. 17: (a) Dynamic response of the inverter following a line tripping event, Initial SCR = 5 (b) FFT Analysis of the RMS voltage measurements.

reduction in the system's strength. Responses of the inverter when the SCR decreases from 5 to 4, 3, and 2, are shown in Fig. 17a. The oscillation magnitude is significantly higher when the SCR changes from 5 to 2. We also discern that the SSO magnitude negatively correlates with the SCR.

It has been observed that the voltage, real power, and reactive power have sustained oscillations. Although we have presented one-second data of the transient simulation, it was noticed that the oscillations never seem to damp out even after 15 seconds of time-domain simulation. The EMT simulation results verify the stability analysis results.

Further, fast Fourier transform (FFT) analysis of the RMS voltage is performed to verify the oscillation frequency and, from Fig.17b, the most dominant frequency for SCR = 4, 3, and 2 are 20, 19, and 18 Hz, respectively. This confirms the veracity of the singular value plots where we observe a
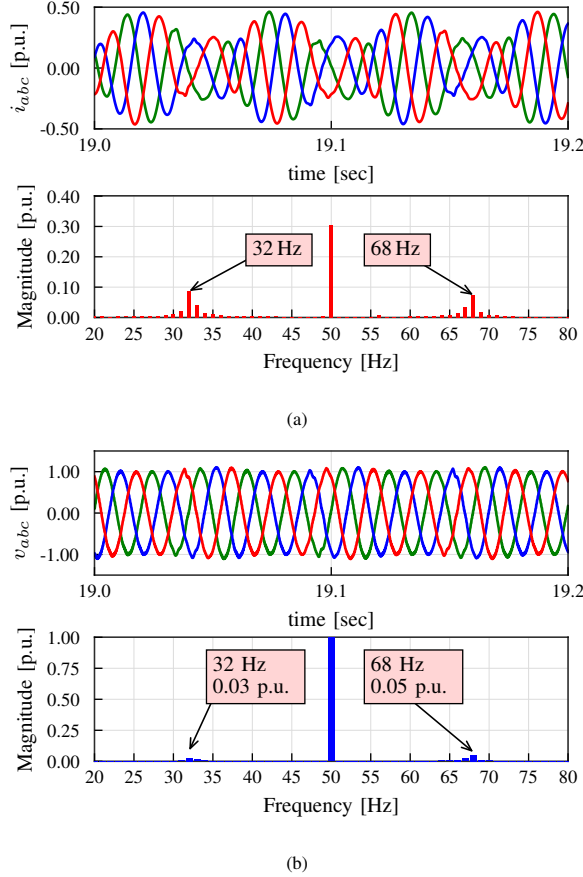
Fig. 18: Transient responses when SCR is 2: (a) Three-phase AC current and FFT analysis of the phase current, (b) Three-phase AC voltage and FFT analysis of the phase voltage.

minimum value around the SSO frequency. Fig. 18a and 18b show the instantaneous current and the voltage measurements when SCR is 2. The phase current has sideband oscillation at frequencies, $f_s \pm f_n = 50 \pm 18 = 32, 68$ Hz. And the magnitude is similar to the dominant oscillation frequency component of the RMS voltage, Fig.17b. In [29], similar observations were made when the oscillations originated from the dq frame control and PLL.

V. CONCLUSION

DQ admittance-based small-signal stability analysis offers a unique advantage since it requires only measurement data rather than a transparent model. Moreover, the measurement can be produced through experiments. We have demonstrated the methods to measure admittance as well as the analysis methods. To achieve accuracy, for each objective, different methods have been applied for cross validation. Both shunt current injection and series voltage injection have been used to create perturbations and identify admittance. Both open-loop gain-based and the return difference matrix-based analysis methods have been applied and shown to deliver the same results that have been further verified by EMT simulation results. It can be seen this measurement-based stability analysis approach offers system operators a tool of high practical value for SSO analysis. This stability analysis tool successfully

pointed out the influencing factors pertaining to the real-world SSO event as the grid strength and the solar irradiation.

REFERENCES

[1] Y. Cheng, L. Fan, J. Rose, S.-H. Huang, J. Schmall, X. Wang, X. Xie, J. Shair, J. R. Ramamurthy, N. Modi, C. Li, C. Wang, S. Shah, B. Pal, Z. Miao, A. Isaacs, J. Mahseredjian, and J. Zhou, "Real-world subsynchronous oscillation events in power grids with high penetrations of inverter-based resources," *IEEE Transactions on Power Systems*, vol. 38, no. 1, pp. 316–330, 2023.

[2] L. Fan, Z. Miao, D. Ramasubramanian, and H. Ding, "Operational challenges of solar PV plus storage power plants and modeling recommendations," *IEEE Open Access Journal of Power and Energy*, 2023.

[3] L. Fan, "Modeling type-4 wind in weak grids," *IEEE Transactions on Sustainable Energy*, vol. 10, no. 2, pp. 853–864, 2019.

[4] A. Yazdani and P. P. Dash, "A control methodology and characterization of dynamics for a photovoltaic (pv) system interfaced with a distribution network," *IEEE Transactions on Power Delivery*, vol. 24, no. 3, pp. 1538–1551, 2009.

[5] J. Undrill and T. Kostyniak, "Subsynchronous oscillations part 1 comprehensive system stability analysis," *IEEE Transactions on Power Apparatus and Systems*, vol. 95, no. 4, pp. 1446–1455, 1976.

[6] B. Badrzadeh, M. Sahni, Y. Zhou, D. Muthumuni, and A. Gole, "General methodology for analysis of sub-synchronous interaction in wind power plants," *IEEE Transactions on Power Systems*, vol. 28, no. 2, pp. 1858–1869, 2013.

[7] L. Fan and Z. Miao, "Nyquist-stability-criterion-based SSR explanation for type-3 wind generators," *IEEE Transactions on Energy Conversion*, vol. 27, no. 3, pp. 807–809, 2012.

[8] B. Gustavsen and A. Semlyen, "Rational approximation of frequency domain responses by vector fitting," *IEEE Transactions on power delivery*, vol. 14, no. 3, pp. 1052–1061, 1999.

[9] M. Zhang, Z. Miao, L. Fan, and S. Shah, "Data-driven interarea oscillation analysis for a 100% IBR-penetrated power grid," *IEEE Open Access Journal of Power and Energy*, vol. 10, pp. 93–103, 2022.

[10] B. Wen, D. Boroyevich, R. Burgos, P. Mattavelli, and Z. Shen, "Small-signal stability analysis of three-phase ac systems in the presence of constant power loads based on measured d-q frame impedances," *IEEE Transactions on Power Electronics*, vol. 30, no. 10, pp. 5952–5963, 2015.

[11] M. Amin and M. Molinas, "Small-signal stability assessment of power electronics based power systems: A discussion of impedance- and eigenvalue-based methods," *IEEE Transactions on Industry Applications*, vol. 53, no. 5, pp. 5014–5030, 2017.

[12] B. Wen, D. Dong, D. Boroyevich, R. Burgos, P. Mattavelli, and Z. Shen, "Impedance-based analysis of grid-synchronization stability for three-phase paralleled converters," *IEEE Transactions on Power Electronics*, vol. 31, no. 1, pp. 26–38, 2016.

[13] N. Modi, E. M. Farahani, A. Jalali, J. Ramamurthy, C. Chin, and B. Soetantijo, "Replication of real-world sub-synchronous oscillations in inverter-based resources dominated grid," *IEEE Transactions on Power Delivery*, vol. 39, no. 3, pp. 1399–1406, 2024.

[14] S. Liu and R. A. Dougal, "Dynamic multiphysics model for solar array," *IEEE Transactions on Energy Conversion*, vol. 17, no. 2, pp. 285–294, 2002.

[15] Z. Shen, M. Jaksic, B. Zhou, P. Mattavelli, D. Boroyevich, J. Verhulst, and M. Belkhayat, "Analysis of phase locked loop (pll) influence on dq impedance measurement in three-phase ac systems," in *2013 Twenty-Eighth Annual IEEE Applied Power Electronics Conference and Exposition (APEC)*, 2013, pp. 939–945.

[16] H. Gong, D. Yang, and X. Wang, "Impact analysis and mitigation of synchronization dynamics for dq impedance measurement," *IEEE transactions on power electronics*, vol. 34, no. 9, pp. 8797–8807, 2018.

[17] Y. Familiant, K. Corzine, J. Huang, and M. Belkhayat, "Ac impedance measurement techniques," in *IEEE International Conference on Electric Machines and Drives, 2005.*, 2005, pp. 1850–1857.

[18] G. Francis, R. Burgos, D. Boroyevich, F. Wang, and K. Karimi, "An algorithm and implementation system for measuring impedance in the d-q domain," in *2011 IEEE Energy Conversion Congress and Exposition*, 2011, pp. 3221–3228.

[19] M. M. H. Garnier and A. Richard, "Continuous-time model identification from sampled data: Implementation issues and performance evaluation," *International Journal of Control*, vol. 76, no. 13, pp. 1337–1357, 2003. [Online]. Available: https://doi.org/10.1080/0020717031000149636

[20] L. Harnefors, "Frequency-domain passivity-based current controller design," *IET Power Electronics*, vol. 1, pp. 455–465(10), December 2008. [Online]. Available: https://digital-library.theiet.org/content/journals/10.1049/iet-pel_20070286

[21] L. Harnefors, M. Bongiorno, and S. Lundberg, "Input-admittance calculation and shaping for controlled voltage-source converters," *IEEE Transactions on Industrial Electronics*, vol. 54, no. 6, pp. 3323–3334, 2007.

[22] M. Beza and M. Bongiorno, "On the risk for subsynchronous control interaction in type 4 based wind farms," *IEEE Transactions on Sustainable Energy*, vol. 10, no. 3, pp. 1410–1418, 2019.

[23] M. Belkhayat, "Stability criteria for ac power systems with regulated loads," Ph.D. dissertation, 1997. [Online]. Available: https://www.proquest.com/dissertations-theses/stability-criteria-ac-power-systems-with/docview/304373829/se-2

[24] L. Fan and Z. Miao, "Admittance-based stability analysis: Bode Plots, Nyquist Diagrams or Eigenvalue Analysis?" *IEEE Transactions on Power Systems*, vol. 35, no. 4, pp. 3312–3315, 2020.

[25] M. Safonov, A. Laub, and G. Hartmann, "Feedback properties of multivariable systems: The role and use of the return difference matrix," *IEEE Transactions on Automatic Control*, vol. 26, no. 1, pp. 47–65, 1981.

[26] L. Piyasinghe, Z. Miao, J. Khazaei, and L. Fan, "Impedance Model-Based SSR Analysis for TCSC Compensated Type-3 Wind Energy Delivery Systems," *IEEE Transactions on Sustainable Energy*, vol. 6, no. 1, pp. 179–187, 2015.

[27] W. Cao, Y. Ma, L. Yang, F. Wang, and L. M. Tolbert, "D–q impedance based stability analysis and parameter design of three-phase inverter-based ac power systems," *IEEE Transactions on Industrial Electronics*, vol. 64, no. 7, pp. 6017–6028, 2017.

[28] Z. Miao and L. Fan, "Bessel Functions and Harmonic Components in an Elementary Single-Phase PLL," 5 2023. [Online]. Available: https://www.techrxiv.org/articles/preprint/Bessel_Functions_and_Harmonic_Components_in_an_Elementary_Single-Phase_PLL/22718368

[29] L. Fan, Z. Miao, S. Shah, Y. Cheng, J. Rose, S.-H. Huang, B. Pal, X. Xie, N. Modi, S. Wang, and S. Zhu, "Real-world 20-Hz IBR subsynchronous oscillations: Signatures and mechanism analysis," *IEEE Transactions on Energy Conversion*, vol. 37, no. 4, pp. 2863–2873, 2022.

Zhixin Miao (Senior Member, IEEE) received the B.S.E.E. degree from the Huazhong University of Science and Technology,Wuhan, China, in 1992, the M.S.E.E. degree from the Graduate School, Nanjing Automation Research Institute (Nanjing, China) in 1997, and the Ph.D. degree in electrical engineering from West Virginia University, Morgantown, in 2002.

Currently, he is with the University of South Florida (USF), Tampa. Prior to joining USF in 2009, he was with the Transmission Asset Management Department with Midwest ISO, St. Paul, MN, from 2002 to 2009. His research interests include power system stability, microgrids, and renewable energy. Dr. Miao serves as an associate editor for IEEE trans. Sustainable Energy.

Lingling Fan (Fellow, IEEE) received the B.S. and M.S. degrees in electrical engineering from Southeast University, Nanjing, China, in 1994 and 1997, respectively, and the Ph.D. degree in electrical engineering from West Virginia University, Morgantown, in 2001.

Currently, she is a full professor with the University of South Florida, Tampa, where she has been since 2009. She was a Senior Engineer in the Transmission Asset Management Department, Midwest ISO, St. Paul, MN, form 2001 to 2007, and an Assistant Professor with North Dakota State University, Fargo, from 2007 to 2009. Her research interests include power systems and power electronics. Dr. Fan serves as Editor-in-Chief for IEEE Electrification Magazine and Associate Editor for IEEE trans. Energy Conversion.

Rahul Halugudde Ramakrishna (Graduate Student Member, IEEE) received the B.E degree from the Ramaiah Institute of Technology, Bangalore India in 2016 and Master of Science degree from the University of South Florida (USF) in 2019. Rahul is presently a Ph.D. candidate at the Smart Grid Power Systems Lab at USF. His research interests include electromagnetic transient computer simulation for inverter-based resource generator interconnection.